1-1-2014

In-situ neutron diffraction of LaCoO3 perovskite under uniaxial compression. I. Crystal structure analysis and texture development

Amjad Aman
University of Central Florida

Yan Chen
University of Central Florida

Mykola Lugovy
University of Central Florida

Nina Orlovskaya
University of Central Florida

Michael J. Reece

Authors

Amjad Aman, Yan Chen, Mykola Lugovy, Nina Orlovskaya, Michael J. Reece, Dong Ma, Alexandru D. Stocia, and Ke An

Amjad Aman, Yan Chen, Mykola Lugovy, Nina Orlovskaya, Michael J. Reece, Dong Ma, Alexandru D. Stoica, and Ke An

View Online   Export Citation   CrossMark

ARTICLES YOU MAY BE INTERESTED IN

In-situ neutron diffraction of LaCoO₃ perovskite under uniaxial compression. I. Crystal structure analysis and texture development

Amjad Aman,[1] Yan Chen,[1,2] Mykola Lugovy,[1,3] Nina Orlovskaya,[1,a)] Michael J. Reece,[4]
Dong Ma,[2] Alexandru D. Stoica,[2] and Ke An[2]

[1]*Department of Mechanical and Aerospace Engineering, University of Central Florida, Orlando,
Florida 32816, USA*
[2]*Chemical and Engineering Materials Division, Neutron Sciences Directorate,
Oak Ridge National Laboratory, Oak Ridge, Tennessee 37831, USA*
[3]*Institute for Problems of Materials Science, Kiev 03142, Ukraine*
[4]*The School of Engineering and Materials Science, Queen Mary, University of London, London E1 4NS,
United Kingdom*

The dynamics of texture formation, changes in crystal structure, and stress accommodation mechanisms have been studied in perovskite-type $R\bar{3}c$ rhombohedral LaCoO₃ during uniaxial compression using *in-situ* neutron diffraction. The *in-situ* neutron diffraction revealed the complex crystallographic changes causing the texture formation and significant straining along certain crystallographic directions during compression, which are responsible for the appearance of hysteresis and non-linear ferroelastic deformation in the LaCoO₃ perovskite. The irreversible strain after the first loading was connected with the appearance of non-recoverable changes in the intensity ratio of certain crystallographic peaks, causing non-reversible texture formation. However, in the second loading/unloading cycle, the hysteresis loop was closed and no further irrecoverable strain appeared after deformation. The significant texture formation is responsible for an increase in the Young's modulus of LaCoO₃ at high compressive stresses, ranging from 76 GPa at the very beginning of the loading to 194 GPa at 900 MPa at the beginning of the unloading curve. © 2014 AIP Publishing LLC.
[http://dx.doi.org/10.1063/1.4884335]

I. INTRODUCTION

LaCoO₃-based perovskites are very exciting materials demonstrating unique magnetic,[1] electrical,[2] catalytic,[3] and mechanical properties.[4] It was reported that LaCoO₃-based ceramics are brittle materials with fracture toughness values ranging from 1.2 MPa m^{1/2} for pure LaCoO₃ to 1.9 MPa m^{1/2} for La₀.₈Ca₀.₂CoO₃.[5] LaCoO₃-based ceramics do not demonstrate elastic deformation during loading, but rather exhibit ferroelastic behavior with non-linearity and hysteresis,[6] which provides a small toughening mechanism,[7,8] as well as temperature and loading rate dependent deformation.[9] Such strong non-linear deformation presents a problem in determining the strength of LaCoO₃-based ceramics using flexure methods, as it implies an asymmetry of the stress distribution on the tensile and compressive surfaces during bending and, therefore, requires a different approach for the strength calculations.[5] In addition, the calculation of Young's modulus of the material is problematic, as it is difficult or almost impossible to find a linear portion of the stress–strain deformation curve at the beginning of loading and, as a result, the calculated values of the slope might be affected by the deviation from linearity of the stress–strain. Therefore, other techniques, such as natural frequencies or resonant ultrasound spectroscopy, might provide more accurate results to determine Young's moduli of ferroelastic ceramics. It was reported that Young's modulus of pure LaCoO₃ is ∼76 GPa at room temperature, as measured using a natural frequencies technique.[5] Very few papers have reported elastic moduli of polycrystalline LaCoO₃[5,10,11] and only one paper has reported the elastic constants of LaCoO₃ single crystal.[12] To the best of our knowledge, no detailed study of the elastic anisotropy of LaCoO₃-based perovskite was performed in the past, as well as no detailed study of changes in the crystal structure, dynamics of texture formation, and stress accommodation were reported in LaCoO₃ during uniaxial compression using *in-situ* neutron diffraction.

The mechanical response of ferroelastic materials is correlated with domain/twin structure and the motion of the ferroelastic domain walls, which, being a thermally activated phenomenon, is time and loading rate dependent.[9,13] The domain structure in LaCoO₃-based perovskites is a consequence of improper transformation from the paraelastic $Pm\bar{3}m$ cubic phase to the ferroelastic $R\bar{3}c$ rhombohedral phase. The $Pm\bar{3}m$-to-$R\bar{3}c$ phase transition is driven by rotation and compression of CoO₆ octahedra about one of the cubic three-fold symmetry axes, which is similar to the transition occurring in LaAlO₃.[14] In the $Pm\bar{3}m$-to-$R\bar{3}c$ transition adjacent octahedral rotate in the opposite way, leading to a doubling of the unit cell along the octahedral rotation axis. The low temperature rhombohedral phase can be described by a non-primitive unit cell with hexagonal lattice vectors[14]

a)Author to whom correspondence should be addressed. Electronic mail:
Nina.Orlovskaya@ucf.edu

$$\begin{pmatrix} a_H \\ b_H \\ c_H \end{pmatrix} = \begin{pmatrix} -1 & 1 & 0 \\ 0 & -1 & 1 \\ 2 & 2 & 2 \end{pmatrix} \begin{pmatrix} a_R \\ b_R \\ c_R \end{pmatrix}.$$

A schematic representation of the rhombohedral LaCoO$_3$ unit cell with presentation of the a_R and α_R along with a_H and c_H lattice parameters, adopted from Ref. 15 is shown in Fig. 1(a). As a result of such a transition, the domains/twins are the dominant microstructural features of lanthanum cobaltites at room temperature,[16–18] which form upon cooling below the transition temperature due to choice of four [111], [1$\bar{1}$1], [$\bar{1}$11], [11$\bar{1}$] equivalent triad axes about which octahedral rotation can occur (Fig. 1(b)).[14] In addition to rhombohedral $R\bar{3}c$ structure, the regions with monoclinic distortion were also reported to exist in LaCoO$_3$ as studied by TEM.[17,18] It was reported that the monoclinic phase also exhibits a ferroelastic behavior.[17,18] It is well known that when a stress is applied to such a twinned crystal, one orientation of the domains/twins remains stable and grows at the expense of the other orientations when a critical coercive stress is surpassed. If the direction of stress is reversed, such that the applied compressive stress is replaced with applied tensile stress during loading, the second structural state becomes stable and the first collapses into the second.[19,20] Such a process is called domain switching/reorientation, which is related to the texturing and formation of preferred orientation during loading of ferroelastic ceramics. The texture formation produces a strong anisotropy in elastic properties of the material.[20] A
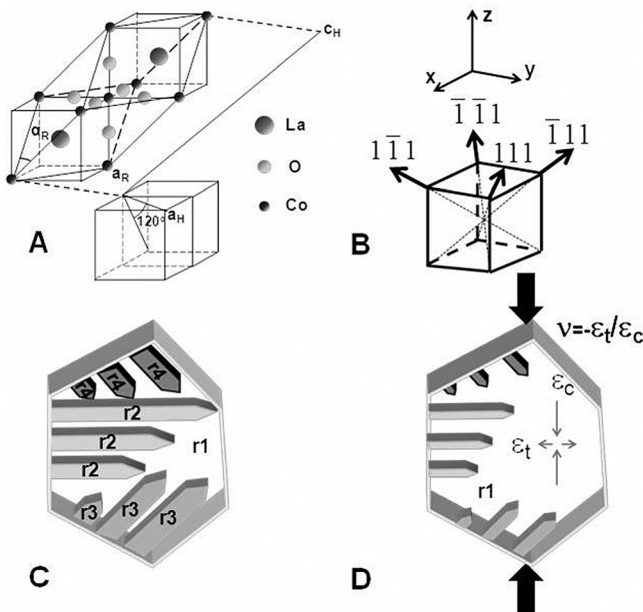

FIG. 1. Schematic presentation of (a) ferroelastic $R\bar{3}c$ LaCoO$_3$ rhombohedral unit cell and its hexagonal representation with relation to the prototype paraelastic cubic structure (a_R and α_R rhombohedral and related a_H and c_H hexagonal lattice parameters are also shown); (b) four types of possible domains in rhombohedral LaCoO$_3$; (c) and (d) ferroelastic strain where all four domain states are present; (c) the grain in an initial untextured state where all four domains have approximately equal volume fractions; (d) when compressive stress is applied, texture will appear and a domain with preferred orientation toward applied stress increases its volume fraction at the expense of domains with other less preferred orientations. The appearance of compressive and tensile strains is also shown.

schematic representation of the domain switching/texturing during compression, adopted from Ref. 21, is shown in Figs. 1(c) and 1(d). Before loading, the grain is isotropic, no texture and four domain states are present (Fig. 1(c)). However, preferred orientation and texture will develop at the expense of the volume fraction increase in one of the domains as well as simultaneous decrease, up to the point of complete disappearance, of other directions when stress is applied. The texture saturation is achieved when the domains of non-preferred orientation disappear at high applied stresses.[22] It is worth noting that uniaxial compressive stress produces a compressive strain ε_c in the direction parallel to the applied stress, and a tensile strain ε_t in the direction normal to the applied stress due to Poisson's effect, where their ratio will provide the value of Poisson's ratio of the isotropic polycrystalline material $\nu = -\varepsilon_t/\varepsilon_c$.

The *in-situ* investigation of domains/twins movements in La$_{0.8}$Ca$_{0.2}$CoO$_3$ perovskite during uniaxial compression has previously been performed using synchrotron X-ray diffraction.[21] It was reported that a ferroelastic texture developed under applied load, and the mechanisms of formation of preferred orientation were discussed. The conclusion was that strain induced by uniaxial compression was not homogeneously distributed in the polycrystalline La$_{0.8}$Ca$_{0.2}$CoO$_3$ due to crystal anisotropy. However, only La$_{0.8}$Ca$_{0.2}$CoO$_3$ perovskite was investigated and no strain analysis of different crystallographic planes during compression was performed. Pure LaCoO$_3$ perovskite has not been studied, but it exhibits different ferroelastic and time dependent behavior in comparison with lanthanum cobaltite doped with 20 at. % of Ca on the A-site.[4] Therefore, the goal of the current research is to study the dynamics of texture development as well as to report the stress accommodation mechanisms during deformation of pure LaCoO$_3$ under uniaxial compression utilizing *in-situ* neutron diffraction.

II. EXPERIMENTAL

Polycrystalline pure LaCoO$_3$ ceramic samples were produced by Praxair Surface Technologies, Specialty Ceramics. For the sample under investigation, the average measured grain size is 2–5 μm and the measured porosity is 4%. It is a single phase material without detectable secondary phase as determined by neutron diffraction. Cylinders with dimensions ø 6 mm and 12 mm length were machined by PremaTech Ceramics to be used for neutron diffraction experiments.

A schematic of the experimental set up used for the uniaxial compression at the VULCAN diffractometer at the Spallation Neutron Source (SNS) is shown in Fig. 2(a). With a time-of-flight, white incident beam spectrum, diffraction peaks over a 0.5–2.5 Å bandwidth of d-spacing are measured by running two double-disk choppers at 30 Hz speed with a nominal 800 kW source power level. The −90° (Bank 1) and +90° (Bank 2) detector banks record neutrons diffracted from the (hkl) crystal planes whose plane normals are parallel to the Q$_1$ and Q$_2$ directions, respectively.[23,24] If there is no texture, the data from both detector banks can be summed. Otherwise, the data from different banks can be used to identify texture information or grain orientation
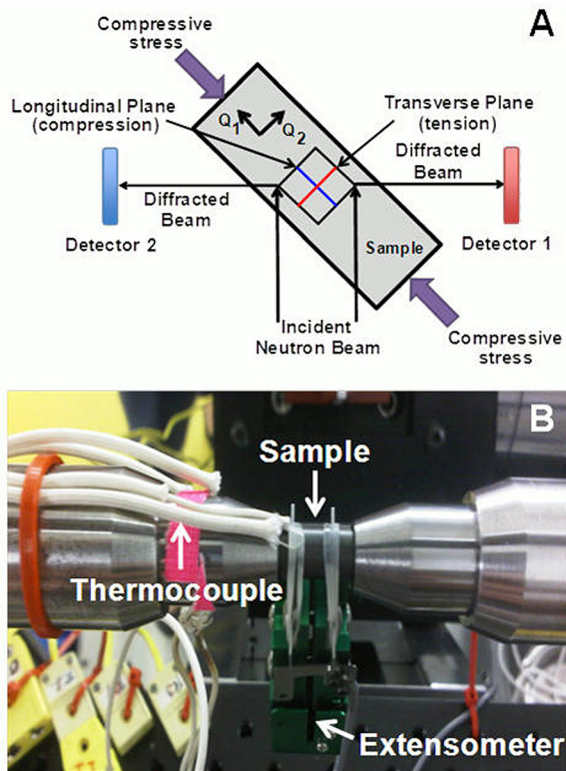
FIG. 2. VULCAN diffractometer set up for *in-situ* neutron diffraction measurements during uniaxial compression. (a) A schematic of neutron diffraction experiment. Plane 1 identified in (a) undergoes compressive deformation during loading. Plane 2 undergoes tensile deformation. The ratio of ε_t and ε_c provides the value of Poisson's ratio, υ, of polycrystalline LaCoO$_3$, such that $\upsilon = -\varepsilon_t/\varepsilon_c$ (b) A photograph of the experimental set up, showing LaCoO$_3$ specimen positioned between two platens. The extensometer is attached to measure the macroscopic strain and three thermocouples are also visible used to measure the temperature of the sample surface, the platen surface and air in the laboratory.

anisotropy. The neutron diffraction measurements were performed in the high-intensity (HI) mode with an instrument resolution of 0.45%. An incident slit of 5 mm width and 3 mm height, with a pair of 5 mm radial collimators, were used together, resulting in a 75 mm^3 gauge volume.

The samples were loaded between two parallel compression platens and an extensometer with a nominal gauge length of 9 mm was used to measure the macroscopic strains. In order to prevent a possible transfer of thermal energy from the machine to the sample, water recirculation was employed within the compression platens to ensure that the platens maintained a constant plant water temperature during the tests. Three thermocouples (Type K, Omega Engineering) were employed to measure temperature at three locations: (i) one thermocouple was attached to the sample's surface to record its temperature during the compression experiments; (ii) another thermocouple was attached to the platen's surface to confirm the temperature of the water cooled platens; and (iii) the last thermocouple was designated to measure the temperature of the environment near the sample, to record any change in ambient temperature, if any. The sample was preloaded in compression with an attached extensometer and three thermocouples as shown in Fig. 2(b).

At SNS, each collected neutron carries a time stamp by the event-based data acquisition mode,[25] and the *in-situ*

neutron diffraction data were collected continuously while loads were applied. The loading and unloading experiments were performed in the load control mode with a loading rate of −1.3 MPa/min until −200 MPa and then the loading rate was increased to −7 MPa/min, and then loading until −900 MPa, unloading till −5 MPa, and further loading till −700 MPa followed by unloading till −5 MPa. The load-frame and neutron data slicing, synchronization, and single peak fitting were performed using the VDRIVE software.[26] The collection of the data lasted for 675 min and 5 min data slicing was chosen based on the diffraction statistics, so a total of 135 diffraction patterns were sliced from the set of collected experimental data.

III. RESULTS AND DISCUSSION

A. Macroscopic measurements of deformation

The stress versus time as well as the resulting macroscopic strain versus time diagrams collected during loading of LaCoO$_3$ perovskite is presented in Fig. 3(a), and the temperature measurements taken during the experiment are presented in Fig. 3(b). As one can see from Fig. 3(a), the stress is applied at constant rates; however, the resulting strain is non-linear, which is an indication of ferroelastic domain wall movement. The temperature measurements indicated that while the air temperature in the laboratory measured close to
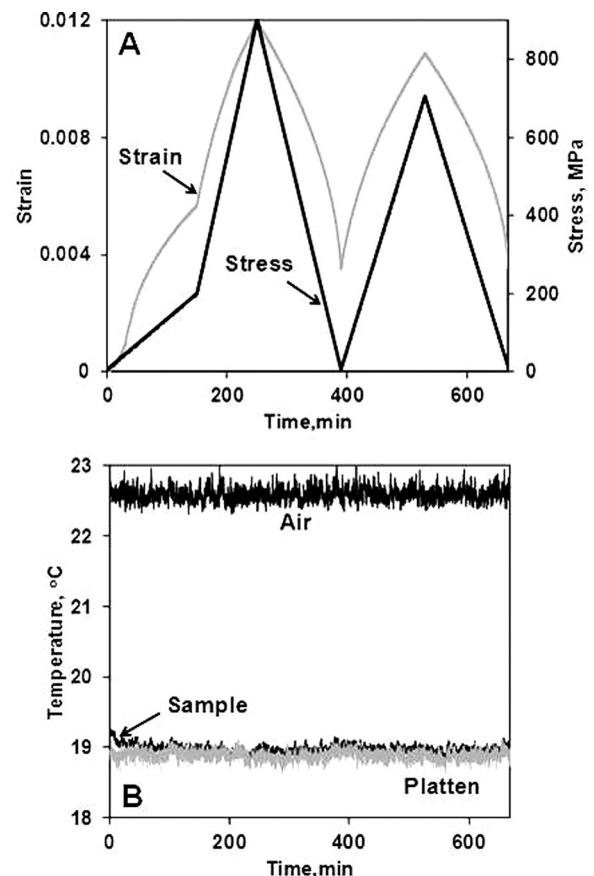

FIG. 3. (a) Stress and macroscopic strain measurements by the extensometer as a function of time; (b) temperature measurements during the experiment showing the temperature of the sample, the platen, and the air in the vicinity of the sample.

the sample's surface was 23 °C for the whole duration of the experiment, the temperature of the water cooled plattens was 19 °C and the sample's temperature was also 19 °C. This indicates that there was a transfer of higher thermal energy from the sample to the push rods at the beginning and during the experiment to keep the sample's temperature constant and independent of the surrounding environment. From the obtained stress and strain versus time data, the resulting stress-strain deformation plots were created. Similar to the previously reported results in Refs. 5 and 7, the ferroelastic hysteretic behavior of $LaCoO_3$ can be detected and the stress-strain deformation plots for the first and second loading/unloading cycles are presented in Fig. 4. The coercive stress calculated from the stress-strain curve is 68 MPa, the hysteresis area is equal to 0.79 MPa, total maximum strain achieved at 900 MPa maximum stress is equal to 0.012, irreversible strain is equal to 0.0035, and the estimated Young's modulus at the very beginning of the loading is equal to 76 GPa. While it is understood that the ferroelastic contribution to the strain is present from the smallest loads during loading of $LaCoO_3$, which results in a deviation of the stress-strain deformation plot from linearity, yet the measured value of Young's modulus for $LaCoO_3$ lies rather close to the values

reported using other techniques.[5] A significant increase in Young's modulus is detected when the material is loaded to the maximum stress of 900 MPa, where the Young's modulus value increases to 194 GPa as measured from the beginning of the unloading curve.

While the hysteresis area is as large as 0.79 MPa in the first cycle, it drops significantly to 0.12 MPa in the second loading/unloading cycle with the strain being fully reversible (Fig. 4(b)). The loading curve in the second cycle coincides with the unloading curve in the first. Both the inflection point corresponding to the coercive stress and Young's modulus at the beginning of loading cannot be determined in the second cycle in a meaningful way; however, the Young's modulus is calculated to be equal to 184 GPa as measured from the beginning of the second unloading curve at 700 MPa compressive stress. All of the above listed parameters of $LaCoO_3$ are summarized in the Table I.

As one can see from Fig. 4, there is a significant increase in Young's modulus of $LaCoO_3$ upon loading. The appearance of texture and the formation of preferred crystallographic orientation might be one explanation for such an increase, since the rhombohedral $LaCoO_3$ exhibits anisotropy of elastic properties in different crystallographic directions. However, no published results were found where changes in Young's modulus of $LaCoO_3$ were reported as a function of applied load and only few selected publications, where Young's modulus was reported for $LaCoO_3$, are published in the literature.[5,10–12] Therefore, if texture formation at different stress levels can be quantified with the determination of the elastic moduli for major crystallographic directions using *in-situ* neutron diffraction, the changes of Young's modulus in $LaCoO_3$ will be predicted as a function of stress and fraction of preferred crystallographic orientation.

B. Changes during cycling in crystallographic orientations of $LaCoO_3$

The diffraction patterns collected during the 675 min of the *in-situ* neutron diffraction experiments showed that all peaks corresponded to the rhombohedral $R\bar{3}c$ space group and did not show any additional reflections which might indicate the presence of monoclinic distortion or
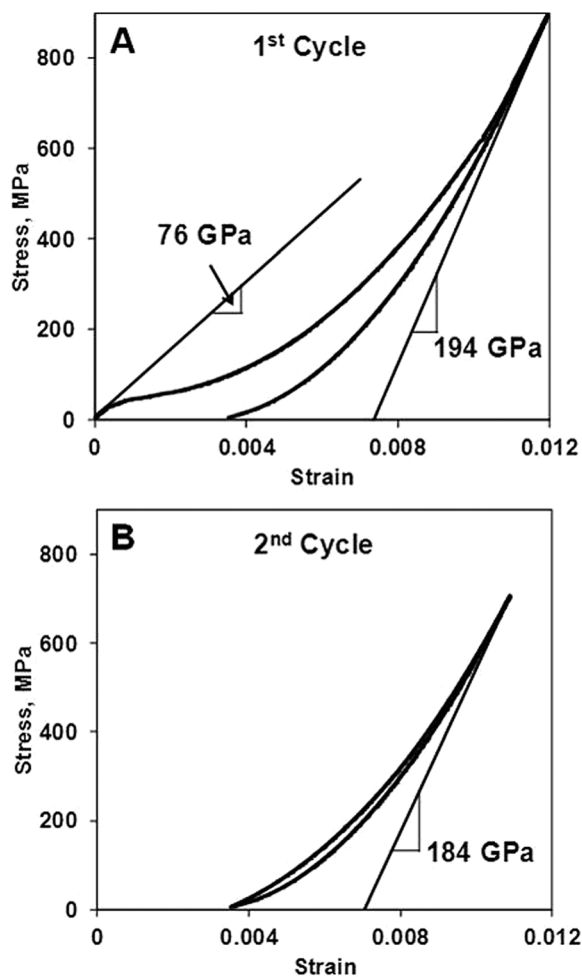

FIG. 4. Stress-strain deformation behavior of $LaCoO_3$. (a) First loading/unloading cycle with a large hysteresis loop and appearance of permanent strain; (b) second loading/unloading cycle with a small and closed hysteresis loop.

TABLE I. Parameters of $LaCoO_3$ from cyclic stress-strain diagram.

| Parameter	Value
Coercive stress, MPa	68
Total maximum strain achieved at 900 MPa maximum stress	0.012
Irreversible strain	0.0035
1st cycle	
Hysteresis area, MPa	0.79
Young's modulus at the very beginning of the loading, GPa	76
Young's modulus measured at the beginning of the unloading curve at 900 MPa applied stress, GPa	194
2nd cycle	
Hysteresis area	0.12
Young's modulus measured at the beginning of the unloading curve at 700 MPa applied stress, GPa	184 GPa
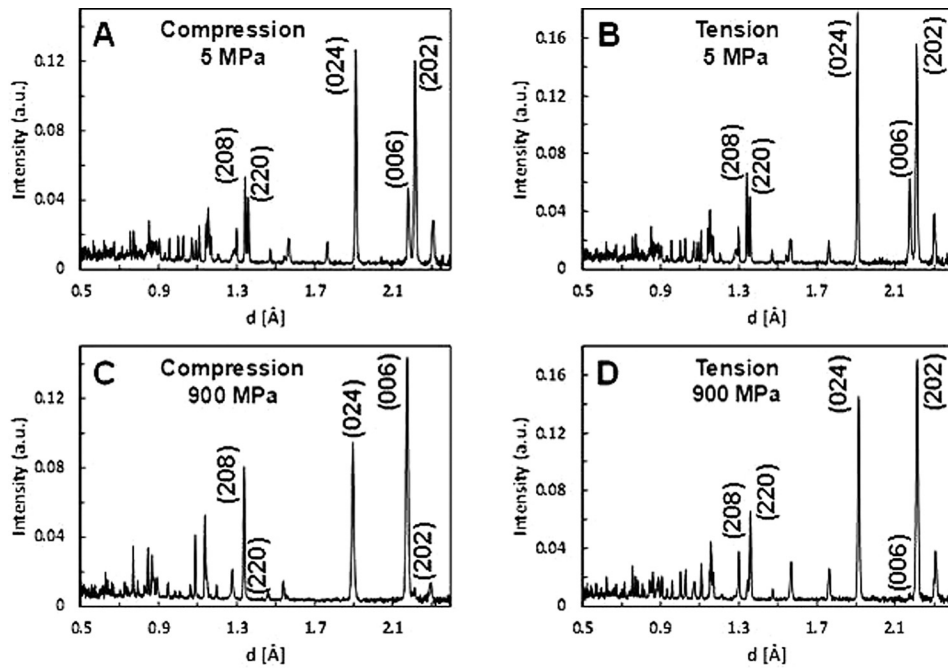
FIG. 5. Neutron diffraction of LaCoO₃ at the beginning of loading (a) and (b) and at 900 MPa compressive stress (c) and (d) as measured by detector 1 (loading direction) (a) and (c) and detector 2 (transversal direction) (b) and (d).

appearance of secondary phases. Fig. 5 presents the diffraction patterns collected at the beginning of the first loading cycle (Figs. 5(a) and 5(b)) and at the highest applied stress of 900 MPa (Figs. 5(c) and 5(d)) with (*hkl*) interplanar spacings exposed to compressive strain (parallel to the applied load) (Figs. 5(a) and 5(c)) and (*hkl*) interplanar spacings under tensile strain (perpendicular to the applied load) (Figs. 5(b) and 5(d)), respectively. Since a significant number of different grains (up to $3 \cdot 10^9$ grains) were used in the collection of diffraction patterns in the radial and lateral direction during loading, statistically we can correlate the data collected by detectors 1 (loading direction) and 2 (transversal direction). As one can see from Figs. 5(a) and 5(b), the material is isotropic at the beginning of loading as the diffraction patterns collected by detectors 1 and 2 are identical. However, almost immediately upon application of stress, different preferred orientations of domains started to appear under the effect of the axial compressive stress or transversal tensile strain, where peak intensities in certain doublets started to decrease up to the point of complete disappearance at high load, while other peak intensities grew at the expense of others. The strong texture developed during uniaxial loading and diffraction patterns of LaCoO₃ with strong preferred orientations are shown in Figs. 5(c) and 5(d). Such strong texture development and formation of the preferred orientation would produce the development of the anisotropic elastic properties and thus be responsible for the increase in Young's modulus of LaCoO₃ at high applied stress. The stress effect on the (024) single peak, (006)/(202) and (208)/(220) doublets are the strongest and the most representative of the LaCoO₃ diffraction patterns will be discussed further in more detail.

C. (024) singlet behavior as a function of applied stress

The behavior of the (024) single peak as a function of applied stress is shown in Fig. 6. The shift to a lower

interplanar spacing, as well as a decrease in intensity and the peak's broadening upon increasing compressive strain is detected by detector 1 (Figs. 6(a) and 6(c)); along with a shift to a higher interplanar spacing, decrease in the intensity and broadening upon increasing tensile strain (Figs. 6(b) and 6(d)). The (024) peak profiles collected by detectors 1 and 2 at the beginning of loading as well at 900 MPa are shown in Figs. 6(a) and 6(b). The 2D presentation of the (024) peak position as a function of applied cyclic stress for detectors 1 and 2 is shown in Figs. 6(c) and 6(d). As one can see from Fig. 6(c), when subjected to compressive strain upon loading, the (024) peak position shifts to the lower interplanar spacing when the applied stress increases up to 900 MPa with simultaneous decrease in intensity of the peak. Upon unloading from 900 MPa to 5 MPa, the (024) peak position shifts back to almost the same *d* value as it was before the beginning of loading and the intensity of the peak is recovered. Upon second loading to maximum compressive stress of 700 MPa, the (024) peak position again shifts to a smaller interplanar distances, but recovers again after unloading. While compressive deformation, which appears in radial direction parallel to the applied load (detector 1), caused the (024) peak position to shift to the smaller interplanar distances, the tensile strain which appears in the transverse direction perpendicular to the applied load (detector 2) causes the (024) peak position to shift to larger interplanar distances (Fig. 6(d)). The tensile deformation also causes peak broadening, and the intensity of the peak decreases at high applied stress, similar to the compressive deformation.

The intensity measured by the height of the peak, full width at half maximum (FWHM), and the area of the (024) peak as a function of applied stress as measured by detectors 1 and 2 are shown in Fig. 7. The intensity, FWHM, and area are all normalized by the initial intensity, FWHM, and area values for (024) peak, respectively, as measured at the beginning of loading. While there is an obvious dependence of
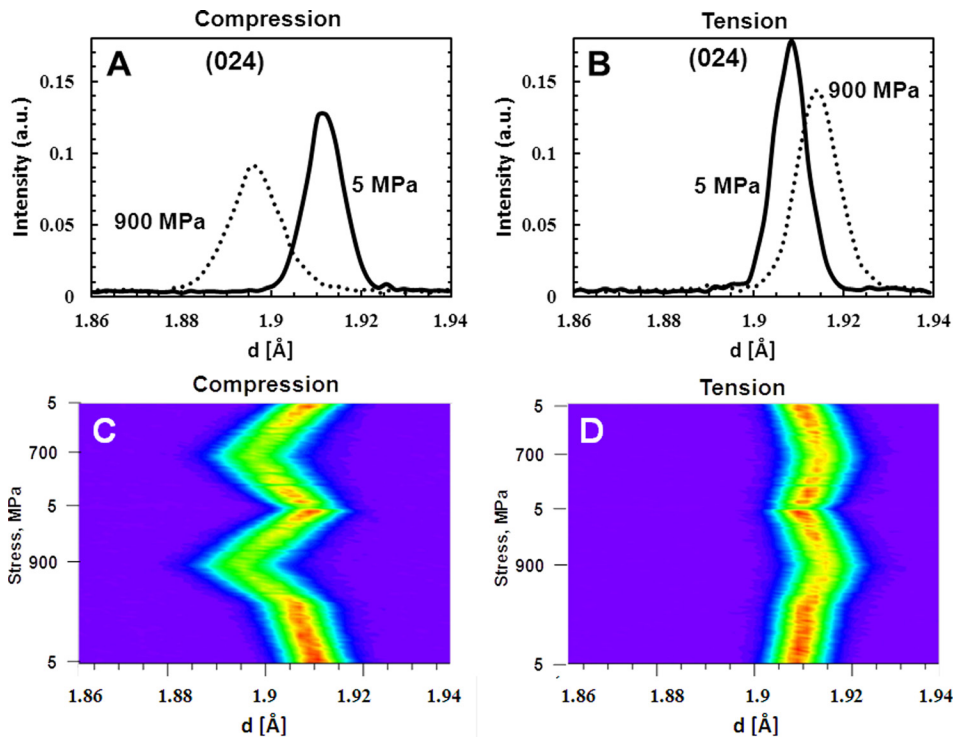
FIG. 6. Diffraction plot of (024) single peak at the beginning of loading and at 900 MPa applied compressive stress (a) and (b). 2D representation of (024) peak's interplanar spacing as a function of applied stress in cycling (c) and (d). The data shown in (a) and (c) were collected using detector 1 and the data shown in (b) and (d) were collected using detector 2.

both intensity and FWHM of the (024) peak as a function of applied stress, the height of the peak is suppressed and the peak broadening is enhanced by the high load, as is expected, however, the intensity of the peak, as represented by the area below the peak, remains constant both for the data collected of detectors 1 and 2 (Figs. 7(e) and 7(f)). In our case, without any detectable structural transition, the intensity (area) of the (024) peak represents the volume fraction of those (024) crystallographic planes whose normal directions are parallel to the diffraction vector. The constant intensity (area) indicates the volume fraction of (024) crystal planes in the particular direction remains constant during the loading/unloading process. Since twinning/domain switching is supposed to be the major mechanism of ferroelastic deformation in LaCoO$_3$, it can be understood that the twin boundaries or the domain walls, which are considered as constant or undeformed planes, lie on the (024) crystallographic plane. The (024) crystal planes thus maintained their original orientation during the entire testing process, although the grains were deformed by twinning/domain switching. The amount of (024) planes in a particular direction did not change, and it led to the independence of peak intensity (area) as a function of applied stress. Detectors 1 and 2 recorded the changes of domain configuration and textures in the LaCoO$_3$ specimen, but the fractions of (024) plane turned out to be constant throughout the loading/ unloading process as recorded by both detectors. However, broadening of the peaks was detected at high loads and such broadening could be explained by the appearance of new domains in the LaCoO$_3$ grains, where the new smaller crystallites contributed to the broadening of the peaks. During the unloading process, the FWHM recovers back to almost its original value, which might indicate the disappearance of the domains when load is removed. The peak height shows
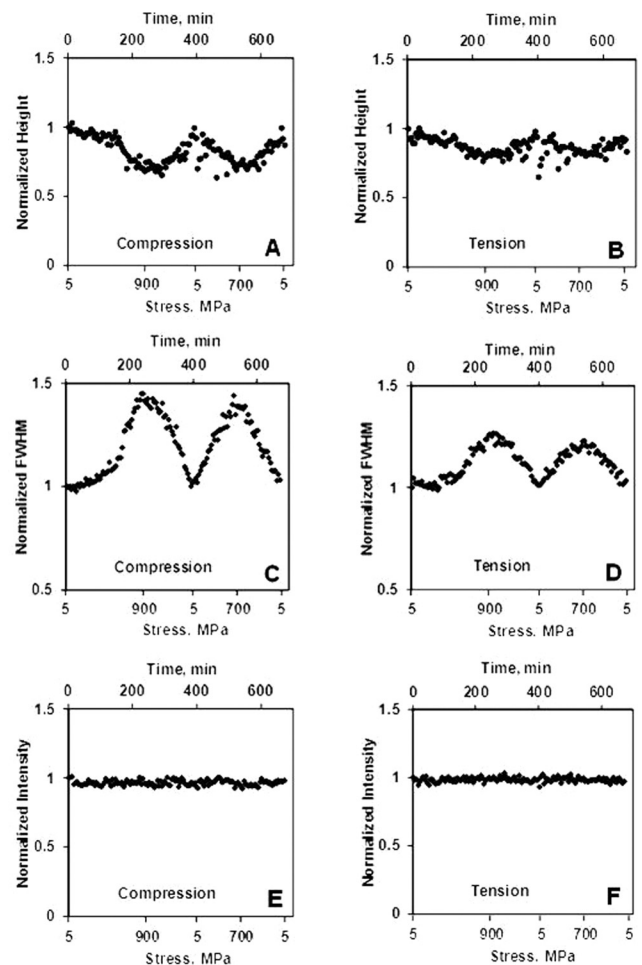

FIG. 7. (024) peak parameters as a function of applied compressive stress. (a) and (b) Intensities measured as the maximum height of the (024) peak; (c) and (d) FWHM; and (e) and (f) intensities measured as the area of the (024) peak. The data presented in (a), (c), and (e) are collected by detector 1 and the data presented in (b), (d), and (f) are collected by detector 2.
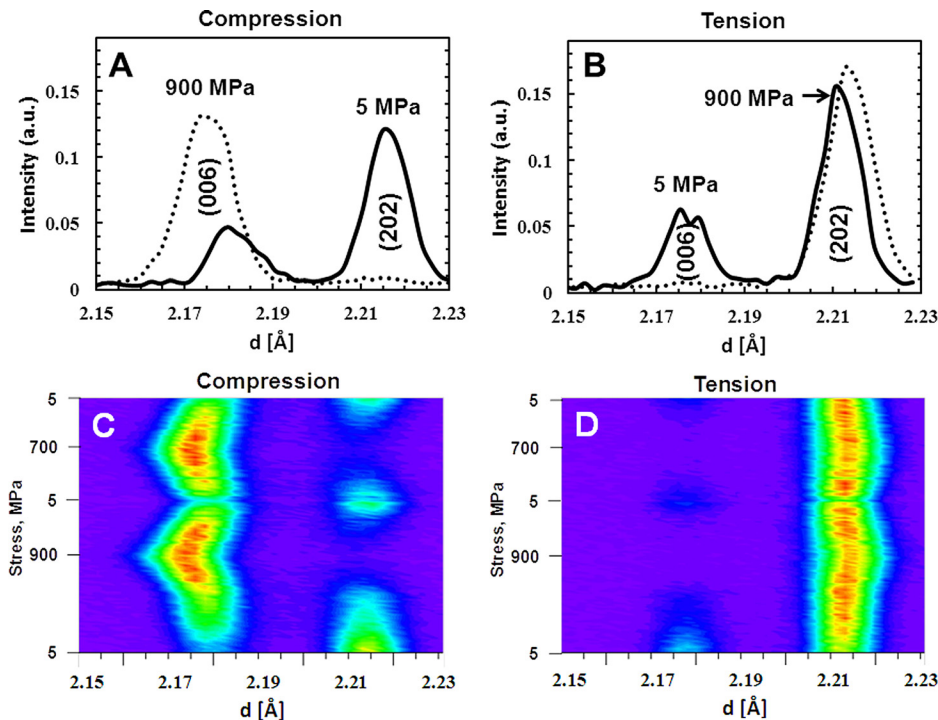
FIG. 8. Diffraction plot of (006)/(202) double peaks at the beginning of loading and at 900 MPa applied compressive stress (a) and (b). 2D representation of (006)/(202) peaks' interplanar spacing as a function of applied stress during cycling (c) and (d). The data presented in (a) and (c) were collected using detector 1 and the data presented in (b) and (d) were collected using detector 2.

an opposite trend compared with FWHM because the peak area remains constant.

D. (006)/(202) and (208)/(220) doublets behavior as a function of applied stress

While the (024) single peak in $LaCoO_3$ only decreases in intensity when stress is applied and never disappears completely at high applied load, the intensities of the doublet peaks change more dramatically (Figs. 8–11). The evolution of the intensities as a function of applied stress depends on the Miller indices of the reflections and the direction of the diffracted neutron beam relative to the stress axis, as it has already been shown in Ref. 21 for $La_{0.8}Ca_{0.2}CoO_3$ perovskite. Similar to the results reported in Ref. 21, the intensity of (202) or (220) peaks decreased in the direction parallel to the stress field upon increasing the load until it completely vanished at a certain applied stress. When stress was removed, the intensities of the (202) and (220) peaks partially recovered, but they never reached the original height that the reflections had prior to loading. Upon second loading, the peaks' intensity decreased again, the peaks vanished again upon loading, but re-appeared upon second unloading. The intensities of the (006) and (208) peaks however behave in the opposite way as they increased with increasing applied stress and their positions shifted to the smaller interplanar distances as the applied compressive stress increased (Figs. 8(a) and 10(a)). The intensity of the (202) or (220) peaks decreased during loading. In the opposite way, the intensities of (006) and (208) peaks increased during loading. Perpendicular to the stress axis, where the tensile strain appears, the intensities of the (202) and (220) peaks increased upon increase in applied stress, but the intensities of the (006) and (208)
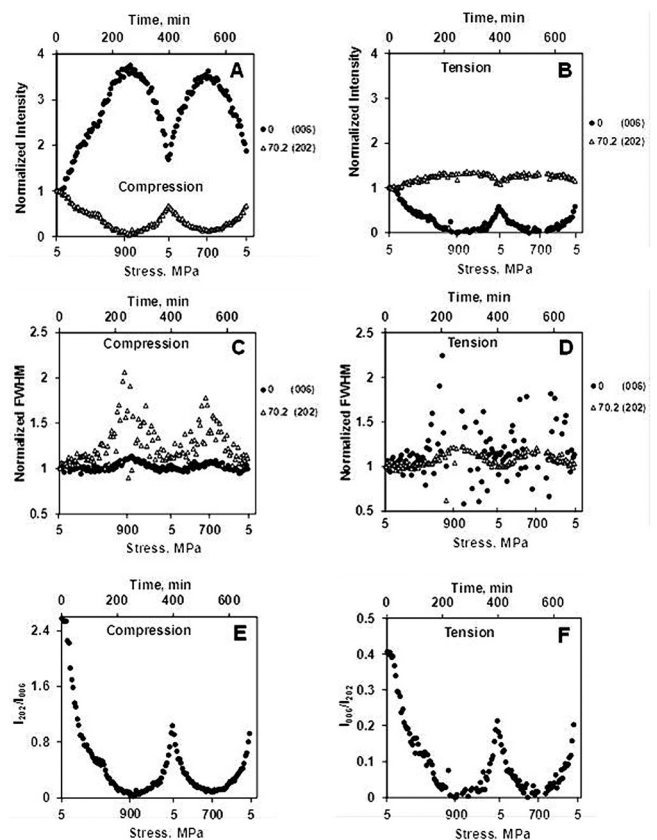

FIG. 9. (006)/(202) peak parameters as a function of applied compressive stress. (a) and (b) Intensities of the peaks are normalized by the intensity of the peaks at the beginning of loading. Here, the intensity represented by the peaks' area; (c) and (d) FWHM; (e) and (f) the intensity ratio of two peaks. The ratio is presented in such a way that the smaller intensity values are placed in the numerator such that the intensity ratio can be presented as zero when the intensity of one of the peaks vanishes. Therefore, I_{202}/I_{006} ratio is presented in (e), but I_{006}/I_{202} ratio is presented in (f). The data presented in (a), (c), and (e) are collected by detector 1 and the data presented in (b), (d), and (f) are collected by detector 2.
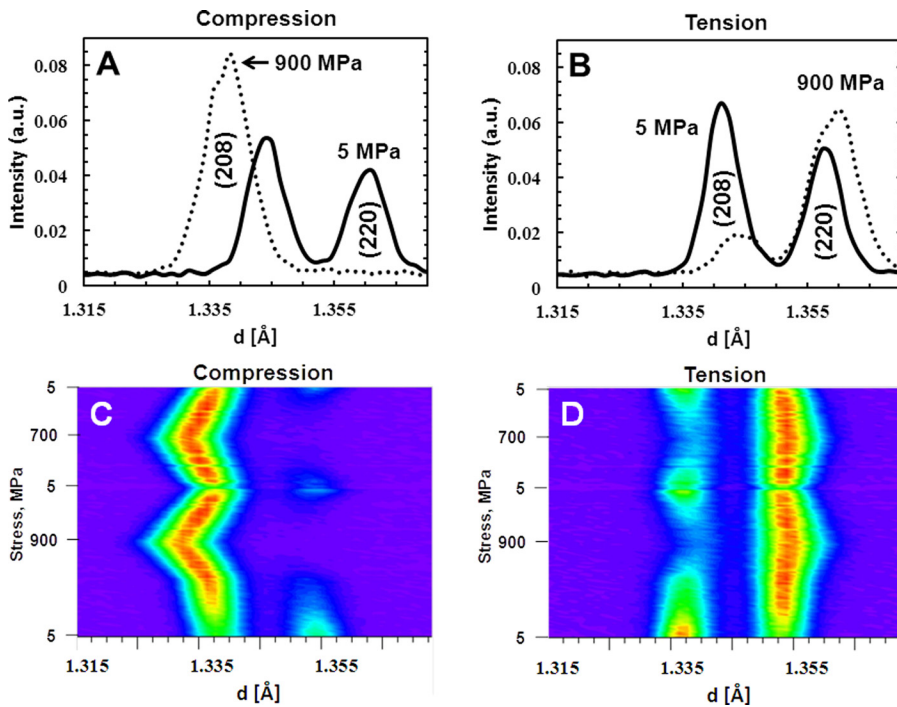
FIG. 10. Diffraction plot of (208)/(220) double peaks at the beginning of loading and at 900 MPa applied compressive stress (a) and (b). 2D representation of (208)/(220) peaks' interplanar spacing as a function of applied stress during cycling (c) and (d). The data presented in (a) and (c) were collected using detector 1 and the data presented in (b) and (d) were collected using detector 2.

peaks decreased and vanished at high stresses. Tensile strain is prevalent for planes oriented parallel to the stress axis, whose corresponding peak positions shift to the higher interplanar spacing when the applied stress is increased (Figs. 8(b) and 10(b)). This is demonstrated well by the changes in the intensities of the (006)/(202) and (208)/(220) peaks as a function of applied stress (Figs. 9(a), 9(b), 11(a), and 11(b)). Both compressive and tensile strains in two orthogonal directions caused a significant broadening of the peaks (Figs. 9(c), 9(d), 11(c), and 11(d)) similar to the broadening observed to occur for the (024) single peak. In order to verify the correlation between the preferred crystallographic orientation and texture formation of the LaCoO$_3$ upon uniaxial compression and the appearance of the hysteresis and macroscopic irreversible strain, the intensity ratios of the (006)/(202) and (208)/(220) peaks were plotted as a function of applied stress (Figs. 9(e), 9(f), 11(e), and 11(f)). As one can see from Figs. 10(e), 10(f), 11(e), and 11(f), the intensity ratios of the doublets decreased rapidly and eventually vanished for the (202)/(006) and (220)/(208) peaks ratio as measured in the axial direction and for the (006)/(202) peaks ratio as measured in the transverse direction. While the intensity ratios of the (208)/(220) peaks did not approach a zero value, it still exhibited a significant decrease when the applied stress increased to 900 MPa as measured in the transverse direction. The inverse ratios of the doublets' intensities were plotted for the data measured by the two detectors to eliminate the problem of using zero intensity values in the denominator. What is immediately visible from the intensity ratio versus applied stress plots is that more than half of the intensity ratios were lost upon first unloading. Although in the first loading/unloading cycle the intensity ratios were not able to recover to their initial values, upon second loading, the intensities of the peaks that disappeared at high
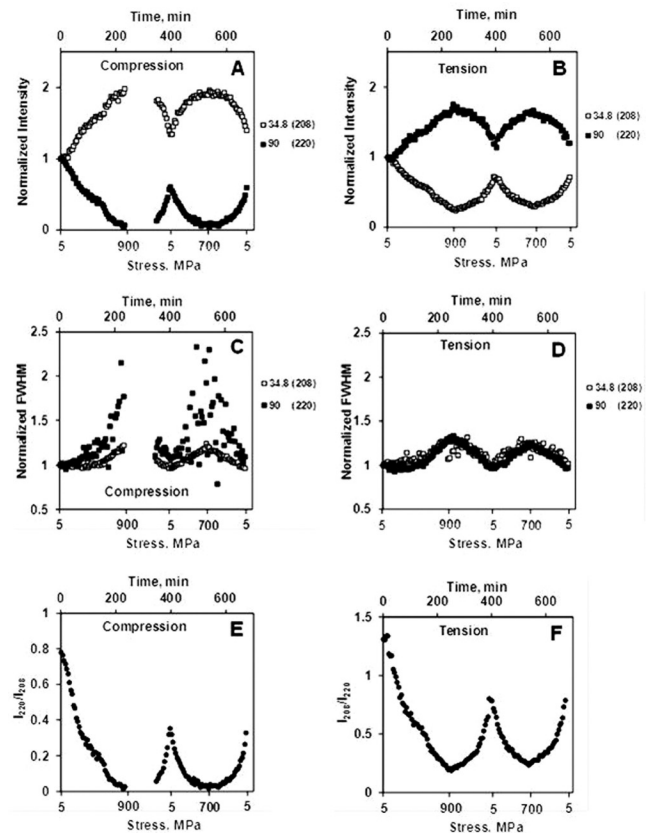

FIG. 11. (208)/(220) peak parameters as a function of applied compressive stress. (a) and (b) Intensities of the peaks are normalized by the intensity of the peaks at the beginning of loading. Here, the intensity is represented by the peaks' area; (c) and (d) FWHM; (e) and (f) the intensity ratio of two peaks. The ratio is presented in such a way that the smaller intensity values are placed in the numerator such that the intensity ratio can be presented as zero when the intensity of one of the peaks vanishes. Therefore, I_{220}/I_{208} ratio is presented in (e), but I_{208}/I_{220} ratio is presented in (f). The data presented in (a), (c), and (e) are collected by detector 1 and the data presented in (b), (d), and (f) are collected by detector 2.

stress level were completely recovered upon second unloading. Thus, upon first loading, irreversible crystallographic changes have been introduced into the structure of isotropic LaCoO$_3$ causing texture formation, and this is

responsible for the appearance of large hysteresis and irreversible strain of the macroscopic stress-strain curve. However, when preferred orientation was already formed, the application of stress caused completely recoverable domains/twin motion and thus the small hysteresis loop that appeared upon second loading/unloading cycle was closed with no permanent strain detected.

E. Accommodation of the lattice strain under uniaxial compression

The lattice strain as a function of applied load determined from the (024), (006)/(202) and (208)/(220) peaks is shown in Fig. 12. The strain of (024) caused by compression, as recorded by detector 1, reached quite a significant value of ~0.008 at 900 MPa, while the value of the maximum tensile strain for the (024) reflection was equal to 0.003 at 900 MPa as measured by detector 2. At the same time, the compressive strain measured for (006)/(202) and (208)/(220) doublets did not reach such high values as was achieved by the compressive lattice strain for a single (024) peak. Both the compressive and tensile strains of double peaks reached only about half of the respective values corresponding to the (024) single peak. The explanation for such large strain appearing by deformation of the single plane is that while doublets can reorient during deformation, and accommodate strain during such reorientation, the single reflection has to react fully to the applied stress as it does not have the strain accommodation mechanisms, which results in much larger deformation and the appearance of higher strain in comparison with the directions where domain switching is possible.

IV. CONCLUSIONS

The crystal structure and texture development in ferroelastic LaCoO$_3$ perovskite under uniaxial compression were studied by *in-situ* neutron diffraction. It was established that while before loading polycrystalline rhombohedral, LaCoO$_3$ is an isotropic ceramic; during the loading process, preferred orientation and texture develop and the material becomes anisotropic. It was also established that during the first loading/unloading cycle, the domain reorientation and texturing was not fully recoverable resulting in the appearance of a significant hysteresis (0.79 MPa) and irreversible permanent macroscopic strain upon unloading. However, during second loading, the domain reorientation was highly recoverable to its original loading state. This produced a much smaller (0.12 MPa) closed hysteresis loop with no observable permanent deformation. The results obtained are important for better understanding of ferroelastic deformation and hysteresis in LaCoO$_3$ perovskite - an important ceramic used in numerous energy-related applications.
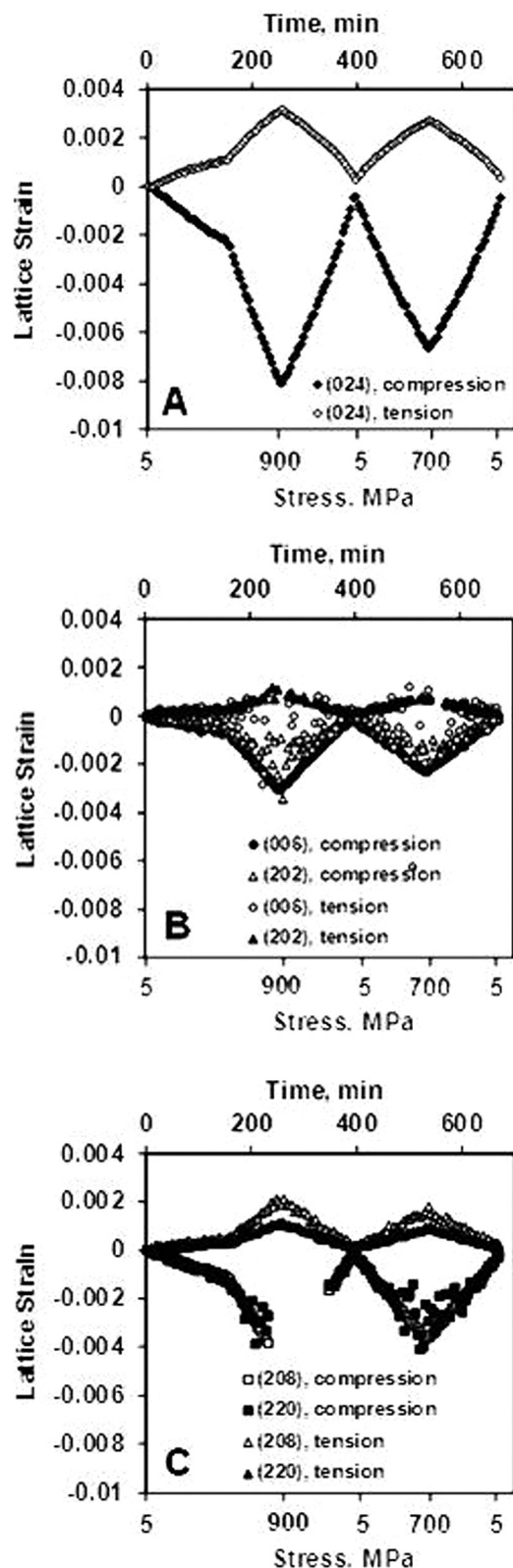

FIG. 12. The lattice strain as a function of applied compressive stress as measured for (024) (a), (006)/(202) (b), and (208)/(220) (c) peaks. The results collected by detectors 1 and 2 are presented.

[1] Q. Wei, T. Zhang, X. P. Wang, and Q. F. Fang, Eur. Phys. J. Appl. Phys. **57**, 30401 (2012).

[2] M. Losurdo, A. Sacchetti, P. Capezzuto, G. Bruno, L. Armelao, D. Barreca, G. Bottaro, A. Gasparotto, C. Maragno, and E. Tondello, Appl. Phys. Lett. **87**, 061909 (2005).

[3] Y. Yamada, K. Yano, D. Hong, and S. Fukuzumi, Phys. Chem. Chem. Phys. **14**, 5753 (2012).

[4] M. Lugovy, V. Slyunyayev, N. Orlovskaya, D. Verbylo, and M. Reece, Phys. Rev. B **78**, 024107 (2008).

[5] N. Orlovskaya, M. Lugovy, S. Pathak, D. Steinmetz, J. Lloyd, L. Fegely, M. Radovic, E. A. Payzant, E. Lara-Curzio, L. Allard, and J. Kuebler, J. Power Sources **182**, 230 (2008).

[6] S. Pathak, J. Kuebler, E. A. Payzant, and N. Orlovskaya, J. Power Sources **195**, 3612 (2010).

[7] N. Orlovskaya, Y. Gogotsi, M. Reece, B. Cheng, and I. Gibson, Acta Mater. **50**, 715 (2002).

[8] M. J. Reece and F. Guiu, Philos. Mag. A **82**, 29 (2002).

[9] S. Faaland, T. Grande, M.-A. Einarsrud, P. E. Vullum, and R. Holmestad, J. Am. Ceram. Soc. **88**, 726 (2005).

[10] J.-S. Zhou, J.-Q. Yan, and J. B. Goodenough, Phys. Rev. B **71**, 220103(R) (2005).

[11] S. Murata, S. Isida, M. Suzuki, Y. Kobayashi, K. Asai, and K. Kohn, Physica B **263–264**, 647 (1999).

[12] T. S. Naing, T. Kobayashi, Y. Kobayashi, M. Suzuki, and K. Asai, J. Phys. Soc. Jpn. **75**, 084601 (2006).

[13] K. B. Chong, F. Guiu, and M. J. Reece, J. Appl. Phys. **103**, 014101 (2008).

[14] R. J. Harrison and S. A. T. Redfern, Phys. Earth Planet. Inter. **134**, 253 (2002).

[15] B. Gilbu, H. Fjellvag, and A. Kjekshus, Acta Chem. Scand. **48**, 37 (1994).

[16] N. Orlovskaya, N. Browning, and A. Nicholls, Acta Mater. **51**, 5063 (2003).

[17] P. E. Vullum, R. Holmestad, H. L. Lein, J. Mastin, M.-A. Einarsrud, and T. Grande, Adv. Mater. **19**, 4399 (2007).

[18] P. E. Vullum, H. L. Lein, M.-A. Einarsrud, T. Grande, and R. Holmestad, Philos. Mag. **88**, 1187 (2008).

[19] K. Aizu, J. Phys. Soc. Jpn. **27**, 387 (1969).

[20] E. K. H. Salje, *Phase Transitions in Ferroelastic and Co-Elastic Crystals, Cambridge Topics in Mineral Physics and Chemistry* (Cambridge University Press, 1990).

[21] P. E. Vullum, J. Mastin, J. Wright, M.-A. Einarsrud, R. Holmestad, and T. Grande, Acta Mater. **54**, 2615 (2006).

[22] J. L. Jones, M. Hoffman, and K. J. Bowman, J. Appl. Phys. **98**, 024115 (2005).

[23] X. L. Wang, T. M. Holden, A. D. Stoica, K. An, H. D. Skorpenske, A. B. Jones, G. Q. Rennich, and E. B. Iverson, Mater. Sci. Forum **652**, 105 (2010).

[24] K. An, H. D. Skorpenske, A. D. Stoica, D. Ma, X. L. Wang, and E. Cakmak, Metall. Mater. Trans., A **42**, 95 (2011).

[25] R. Riedel, "Spallation neutron source data acquisition system," SNS Report No. 107030200-TD005-R04, Oak Ridge National Laboratory, Oak Ridge, TN, 2007.

[26] K. An, "VDRIVE—Data reduction and interactive visualization software for event mode neutron diffraction," Report No. ORNL-TM-2012-621, Oak Ridge National Laboratory, 2012.